Journal of Power Sources 279 (2015) 581–592

Contents lists available at ScienceDirect

Journal of Power Sources

journal homepage: www.elsevier.com/locate/jpowsour

Hierarchical self-assembled structures based on nitrogen-doped carbon nanotubes as advanced negative electrodes for Li-ion batteries and 3D microbatteries

Tiva Sharifi [a, 1], Mario Valvo [b, 1], Eduardo Gracia-Espino [a, c], Robin Sandström [a], Kristina Edström [b, *], Thomas Wågberg [a, *]

[a] Department of Physics, Umeå University, S-901 87 Umeå, Sweden
[b] Department of Chemistry – Ångström Laboratory, Uppsala University, Box 538, S-751 21 Uppsala, Sweden
[c] Department of Chemistry, Umeå University, S-901 87 Umeå, Sweden

HIGHLIGHTS

- Hierarchical self-assembled structures with unique 'tree-like' morphology and functionalities are grown on carbon paper.
- The defective walls of N-doped CNTs provide favorable sites to grow hematite nanorods.
- Increasing Li storage, excellent coulombic and cycle efficiencies are obtained by incorporating N-doped CNTs.
- A thorough electrochemical analysis of the resulting hierarchical structures has been performed.

GRAPHICAL ABSTRACT

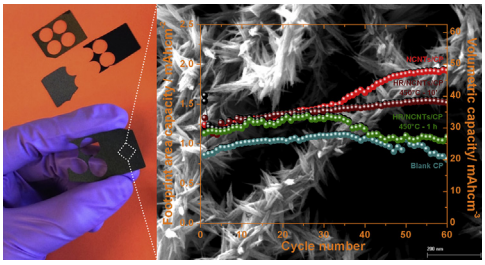

ARTICLE INFO

Article history:
Received 12 October 2014
Received in revised form
3 December 2014
Accepted 6 January 2015
Available online 7 January 2015

Keywords:
Li-ion microbatteries
Nitrogen-doped carbon nanotubes
Hematite
Self-assembly
3D negative electrodes
Carbon paper

ABSTRACT

Hierarchical structures based on carbon paper and multi-walled nitrogen-doped carbon nanotubes were fabricated and subsequently decorated with hematite nanorods to obtain advanced 3D architectures for Li-ion battery negative electrodes. The carbon paper provides a versatile metal-free 3D current collector ensuring a good electrical contact of the active materials to its carbon fiber network. Firstly, the nitrogen-doped carbon nanotubes onto the carbon paper were studied and a high footprint area capacity of 2.1 mAh cm^{-2} at 0.1 mA cm^{-2} was obtained. The Li can be stored in the inter-wall regions of the nanotubes, mediated by the defects formed on their walls by the nitrogen atoms. Secondly, the incorporation of hematite nanorods raised the footprint area capacity to 2.25 mAh cm^{-2} at 0.1 mA cm^{-2}. However, the repeated conversion/de-conversion of Fe_2O_3 limited both coulombic and energy efficiencies for these electrodes, which did not perform as well as those including only the N-doped carbon nanotubes at higher current densities. Thirdly, long-cycling tests showed the robust Li insertion mechanism in these N-doped carbonaceous structures, which yielded an unmatched footprint area capacity

* Corresponding authors.
E-mail address: Thomas.wagberg@physics.umu.se (T. Wågberg).
[1] Equal contribution as first authors.

http://dx.doi.org/10.1016/j.jpowsour.2015.01.036

enhancement up to 1.95 mAh cm^{-2} after 60 cycles at 0.3 mA cm^{-2} and an overall capacity of 204 mAh g^{-1} referred to the mass of the entire electrode.

1. Introduction

Li-ion batteries (LIBs) currently dominate the market of portable electronics and their success has been related to their high energy density and versatility. However, these batteries are challenged in applications requiring increasing levels for both energy and power densities simultaneously, because such condition unavoidably creates a bottleneck [1–4] in conventional laminated electrodes, as well as in thin-film cells.

The use of nanostructures is generally regarded as a viable approach to reduce the path lengths of the charge carriers, while increasing the surface area for the active materials. Although this has a positive impact on the power density, because it improves the reaction kinetics and facilitates the uptake and removal of Li^+ ions and electrons, the energy density of nanomaterials remains inherently limited, due to their low tap density [5,6]. Moreover, the surface area enhancement due to the increased ratio between 'bulk' and 'surface' atoms in nanomaterials often can cause stability problems at the interfaces triggering side reactions [6]. The advantages deriving from the use of nanostructures are in most of the cases spoiled by their difficult or poor assembly into suitable electrodes [7]. In particular, agglomeration is one of the major problems when dispersing and stabilizing nanostructures, due to their high surface energy. In this respect, the idea of a three-dimensional (3D) electrode architecture is attractive, because the individual active nanostructures are directly wired to an extensive electrical network and all the ancillary materials (*i.e.* binders and conductive additives) can be avoided [8]. This raises the energy density of the entire electrode assembly, while retaining the beneficial characteristics of the nanostructured materials and their extended interfaces. 3D electrodes have thus the potential to address the main issues of conventional planar configurations, provided that a suitable matching of the materials ensures a good adhesion between the conductive network and the active component(s), without negating porosity and a quick access to both Li^+ and e^- through the entire structure [3,9]. These characteristics are crucial, especially if miniaturizing the entire battery would impose further limitations on the available space for its various components, which would need to be downscaled as well [2,9].

Recently, multi-walled (MW) nitrogen-doped carbon nanotubes (NCNTs) have attracted attention as an alternative material to graphite for negative electrodes, due to their unique Li storage properties, which significantly differ from those of other similar CNTs [10,11]. Apart from their outstanding electrical and mechanical properties, chemical stability, high aspect ratio and extended surface area, the presence of nitrogen atoms induces the formation of extrinsic defects that act as preferential adsorption sites for Li^+ ions, thus increasing the capacity [11]. This effect acquires a new dimension in NCNTs, because the Li^+ ions are also able to penetrate the defective tube walls and can be stored progressively in the inter-wall regions [11]. The space separating the coaxial tubular structures becomes thus available for Li insertion, enabling the use of their inner interfacial areas, which previously were not accessible. A high concentration of nitrogen doping in CNTs has been shown to positively affect both the reversible capacity and the rate capability [10] for the corresponding electrodes, although other studies show that also low levels of nitrogen doping can enhance the electrochemical activity of CNTs [12]. Theoretical studies of single-walled carbon nanotubes indicate that nitrogen doping should narrow the actual energy band gap for the fraction of semiconductor tubes, while causing electron backscattering for those having a metallic character [13–15]. A recent study shows also that diverse types of nitrogen defects may alter the electronic properties differently [16]. For MW-NCNTs, the presence of nitrogen enhances both the conductivity and the reactivity of the resulting CNTs [17–19], while the nitrogen defects create sites that can interact better with metallic nanoparticles [20,21]. Accordingly, MW-NCNTs could be used as a robust 'reactive scaffolding' to improve the electrochemical properties of other nanostructured materials such as metal oxides, which could grant access to even higher capacities, despite their typical limitations of poor conductivity and cycleability in conventional electrode structures. In particular, a material featuring multi-electron transfer reactions such as iron oxide (e.g. hematite) would be one of the best candidates to test the validity of such approach. Iron oxide undergoes a characteristic conversion reaction at low voltage *vs.* Li^+/Li, which involves the formation of Fe nanoparticles embedded in a Li_2O matrix following the reversible process indicated below [22]:

$$Fe_2O_3 + 6Li^+ + 6e^- \leftrightarrow 3Li_2O + 2Fe \quad (1)$$

This particular electrochemical mechanism generates a theoretical specific capacity of 1007 mAh g^{-1}, which is one of the highest among transition metal oxides (TMOs) undergoing similar reactions. Nevertheless, Fe_2O_3 presents a series of problems, namely; *i.* scarce electronic conductivity, *ii.* agglomeration for its nanoparticulated forms, *iii.* significant volume variation upon lithiation/delithiation (*i.e.* ≈93%), *iv.* poor Coulombic efficiency in the first cycle, *v.* pronounced voltage hysteresis between discharge and charge (*i.e.* low energy efficiency) and, ultimately, *vi.* limited capacity retention. These issues have hindered its practical applications in advanced batteries [23,24]. Different strategies have been applied to partly address these problems, which are common to most of the convertible TMOs. Among others, hybrid nanomaterials [25] combining iron oxide (and other TMOs) with a conductive matrix, such as graphene [26] or CNTs [27] have been utilized to overcome agglomeration problems and buffer the volume changes. In fact, hematite (α-Fe_2O_3) can beneficiate from a direct contact with a conductive support providing a favorable pathway for electron transfer, thus addressing its short carrier diffusion length [28] (a few nanometers). This approach helps reducing the interfacial resistance, thereby improving the capacity retention at high cycling rates [29,30].

One of the main advantages of nanotubes as a conductive network is that they intrinsically offer a high 'surface to volume' ratio, and, since they are made of carbon, they possess a very low density. Still, the main difficulty with hybrid nanomaterials remains, e.g. achieving a solid attachment of the conductive network to the current collector without using any binder or additives, while retaining a superior electrode architecture and integration of each component [31].

With these ideas in mind, the present study focuses on understanding the role of NCNTs to advance the production of 3D negative electrodes for Li-ion batteries, while including additional

functionalities on their reactive surface sites by means of self-assembly techniques. Here, we present a new way of taking advantage of the nitrogen sites in carbon nanotubes to grow hierarchical electrode structures, where highly oriented hematite rods have been attached to the outer walls of the tubes. The idea is to fabricate a copper-free current collector for 3D negative electrodes using carbon paper as a lightweight conducting substrate for the NCNTs. A further goal is to study if this type of electrodes could be down-scaled to match 3D microbattery requirements.

The route presented here is highly reproducible, can be up-scaled and opens the way to the fabrication of these active nanomaterials directly onto the surface of current collectors with a 3D architecture *via* a convenient bottom-up approach. Finally, we show that the carbon paper support does not only provide a conductive network here, but it also behaves as an active material itself.

2. Experimental

2.1. Synthesis of the hierarchical structures

Carbon paper (SIGRACET®GDL 10AA from Ion power, GmbH) having a resistivity below 15 mΩ cm was coated with a 10 nm buffer layer of titanium and then with a thin (~5 nm) catalyst film of iron using a thermal evaporator (Kurt J. Lesker PVD 75). The NCNTs were grown on this substrate by catalytic chemical vapor deposition (CCVD). The system was purged initially with argon (flow rate: 120 mL/min) and heated up to 800 °C. When the set temperature was reached, the carbon paper (CP) substrate was pre-treated by a gas mixture of Varigon™ (flow rate: 110 mL/min) and ammonia (flow rate: 25 mL/min) for 15 min. The Varigon™ flow rate was increased to 120 mL/min, while the ammonia feeding was stopped and pyridine was injected into the reaction chamber with a flow rate of 15 μL/min using a NEMSYS syringe pump (Cetoni GmbH). After 60 min of growth, the system was cooled to room temperature in an argon atmosphere and then the NCNTs/CP was stored for further use. In the next step, 1.24 g of iron trichloride hexahydrate ($FeCl_3.6H_2O$ — Sigma–Aldrich, 0.15 mol/L) and 2.25 g of sodium nitrate ($NaNO_3$ — Fisher Scientific, 1 mol/L) were dissolved in 30 mL of a mixture of deionized water/methanol (1:1) and then poured into a 30 mL autoclave. A piece of NCNTs/CP was placed vertically in the autoclave and maintained at 80 °C for 18 h. The resulting material was washed with water and ethanol several times and then dried at 80 °C over night. Finally, the NCNTs/CP coated with iron hydroxide was transferred to an oven and heat-treated at 450 °C for different times (*i.e.* 10 min and 1 h) in order to form and consolidate the hierarchical hematite nanostructures (HR/NCNTs/CP).

2.2. Characterization of the materials

Scanning electron microscopy (SEM) was performed using a Zeiss Merlin FEG-SEM instrument. TEM was carried out on a JEOL JEM-1230 transmission electron microscope at 80 keV. X-ray diffraction (XRD) was carried out by a Siemens D5000 diffractometer equipped with a Cu-K_α radiation source. The Raman spectroscopy analyses were conducted on a Renishaw InVia Raman spectrometer with a charge-coupled device detector and using a laser excitation wavelength of 633 nm. The X-ray photoemission spectroscopy (XPS) was performed on a Kratos axis ultra delay-line detector electron spectrometer using a monochromatic Al K_α source operated at 150 W. Energy dispersive X-ray spectroscopy (EDX) was carried out by SEM-EDS (Zeiss Merlin FESEM/Oxford Instruments EDS X-Max 80 mm^2) with accelerating voltage of 15 kV, working distance of 8.5 mm, process time of 4, probe current of 300 pA and total duration of 118 s (per analysis). Thermogravimetric analysis (TGA) measurements were done by a METTLER Toledo TGA/DSC-1. Sample were ground completely and then heated up to 950 °C with a heating rate of 5 °/min in an air flow of 30 mL/min.

2.3. Battery assembly and electrochemical measurements

The various electrodes were punched out from their respective carbon paper (CP) supports by means of a precision perforator (Hohsen) for the electrochemical analyses. Their thickness was measured by a digital caliper (Mitutoyo). Circular electrodes with a diameter of 10 mm and an average thickness of 0.4 mm were collected and dried in a vacuum oven (Büchi) at 120 °C for 12 h before cell assembly. The batteries were prepared in an Ar-filled glove box (M-Braun) with oxygen and water levels below 1 ppm. These binder-free electrodes were embedded in Li half-cells and vacuum-sealed in polymer laminated aluminum pouches (*i.e.* 'coffee bags'). Li foil was used as combined reference and counter electrode, while the various CP-based specimens acted as the working electrode. A thin membrane (Solupore) was used as separator in all the cells and it was soaked with a 1 M $LiPF_6$ electrolyte solution in ethylene carbonate and diethyl carbonate (EC:DEC) in a ratio of 1:1. After the electrochemical tests, the cells were opened in the glove box and disassembled in order to remove the cycled electrodes. The latter were carefully washed with dimethyl carbonate (DMC) several times in order to remove the electrolyte salt from the surface of the structures prior to 'post-mortem' SEM analysis.

All the electrochemical analyses (*i.e.* voltammetric measurements and galvanostatic tests) were performed at room temperature *via* a VMP2 (Bio-Logic) equipment. Cyclic voltammetry (CV) was conducted for the respective Li half cells at increasing scan rates between 0.05 and 0.8 mV s^{-1} in a voltage range spanning from 0.05 to 3.0 V *vs.* Li^+/Li. The galvanostatic tests were run at different current densities, *i.e.* 0.1 and 0.3 mA cm^{-2}, corresponding to diverse C-rates. Here the term $n \cdot C$-rate corresponds to the utilization of the entire capacity of each electrode in $1/n$ hours. The performances of the electrodes were assessed mainly in terms of footprint area and volumetric capacities, since it is difficult to discern accurately the contributions of the various active masses in these complex structures. In particular, the CP support displayed an evident electrochemical activity, thus the gravimetric capacities were herein referred to the *total mass* of each electrode embedding all the possible active components.

3. Results and discussion

3.1. Structural and compositional analysis of the hierarchical electrode materials

The synthesis of the hierarchical hybrid materials relied on a bottom up self-assembly process based on the following steps (for details see the experimental section, as well as Fig. 1a-f); i) A titanium buffer layer and an iron catalyst film were evaporated in sequence onto a CP substrate; ii) NCNTs were grown on the CP support by chemical vapor deposition (CVD) using pyridine as C/N precursor in a Varigon™ atmosphere. The resulting structure with NCNTs densely grown out from the carbon fibers of the support (referred to as NCNTs/CP) is shown schematically in Fig. 1d and its morphology is presented in the SEM image in Fig. 1g; iii) Iron hydroxide nanorods were then grown on the surface of the NCNTs *via* a hydrothermal process. This step is similar to the study by de Carvalho et al. [32], however, some modifications were carried out to achieve the growth of highly oriented hematite nanorod arrays on the substrate. Applying similar experimental conditions in the

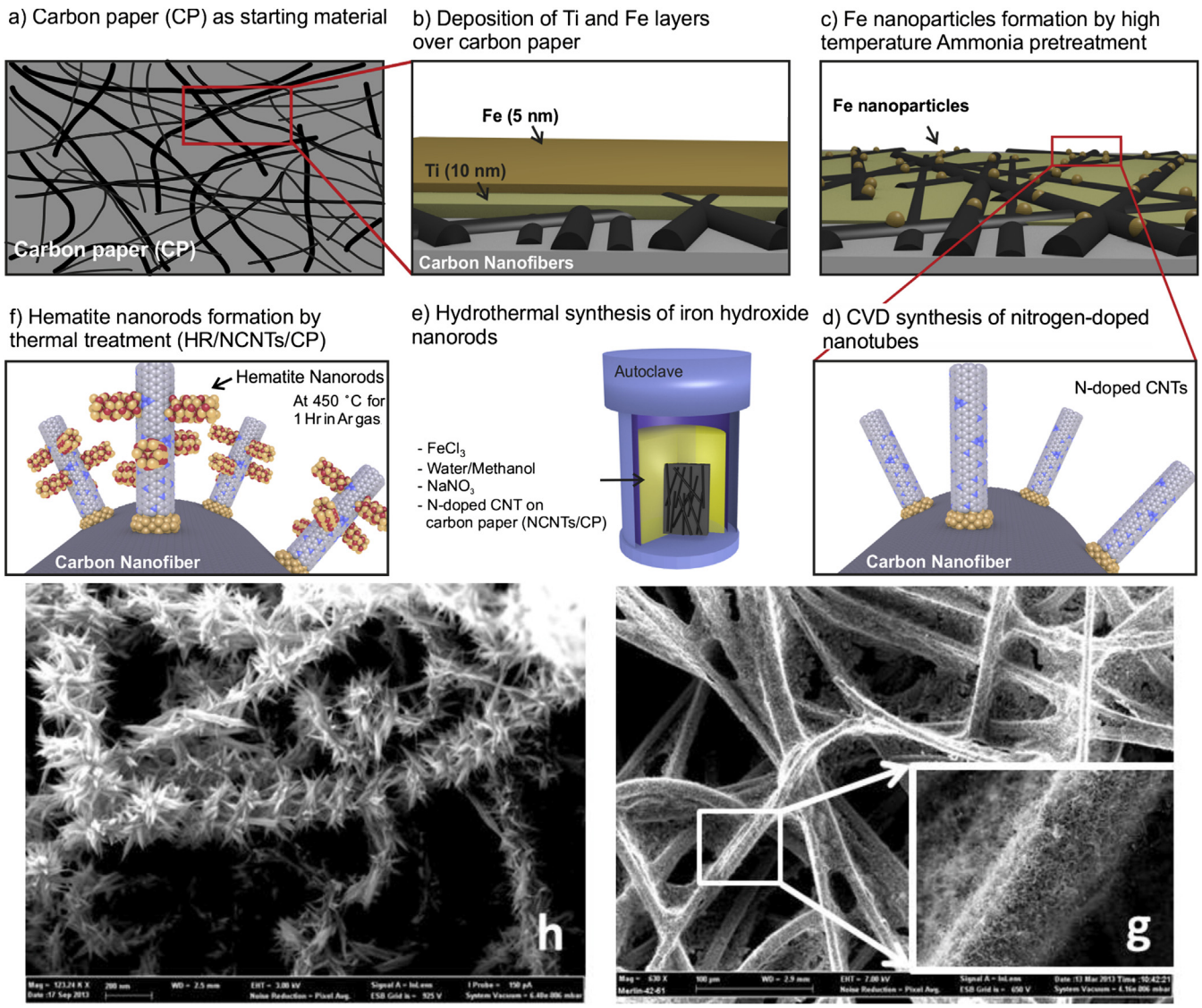

Fig. 1. Schematic picture of the synthesis route to prepare the hierarchical HR/NCNTs/CP structures (a–f) and SEM images of the resulting NCNTs/CP (g) and HR/NCNTs/CP (h) electrodes.

autoclave without including a carbon paper support yields a reduced number of iron hydroxide rods and the latter display also lower quality. This can be rationalized on the basis of the surface properties of the metal oxides, meaning that their interfacial energy and the carbon support promote a higher number of nucleation sites in the presence of a carbon substrate [33]. Furthermore, it is believed that the presence of nitrogen in carbon nanostructures facilitates the nucleation of nanoparticles on their surface in a more effective way than for those not subjected to N-doping [21,34–37]. The introduction of NCNTs as a further extension of the carbon substrate has thus two major advantages; it reduces the interfacial energy of the metal oxide-NCNT system, thereby promoting the vertical growth of hematite nanorods on the NCNTs and provides defects with high adsorption energy for the attachment of these iron oxide nanostructures, as well as for accommodating Li^+ ions upon electrochemical reactions. The growth of iron hydroxide nanorods on NCNTs was confirmed by Raman spectroscopy (see Fig. 2); iv) Iron hydroxide was finally transformed into hematite by a heat treatment in air at 450 °C for different time intervals.

The final structure can be viewed as a low-growing pine tree, where the 'trunk' represents the carbon fibers, the 'branches' the NCNTs and the 'needles' the hematite nanorods, respectively. The schematic structure of the hybrid material and its components are shown in detail in Fig. 1f. Fig. 1h displays the SEM image of the NCNTs decorated by hematite nanorods (HR) grown at 450 °C for 1 h. This hybrid material is from here on referred to as HR/NCNTs/CP for convenience.

Fig. 2 shows the Raman spectrum of the hybrid material after the heat treatment for 1 h at 450 °C, while the inset depicts its spectrum before this process. The spectrum in the inset exhibits features that match well with those characteristic of iron hydroxide [38]. The high wavenumber region in the Raman spectrum of Fig. 2 displays a D-band and a G-band which are characteristic for nitrogen-doped carbon nanostructures [39,40]. The D-band strongly overlaps the intense feature of hematite at high wavenumbers, which is attributed to two-magnons scattering [41] in this antiferromagnetic material, thus giving a very broad appearance for such band. The low wavenumber region of the spectrum is free from nanotube-related features and therefore the characteristic hematite signatures [34,41,42], *i.e.* the distinctive peaks at 224

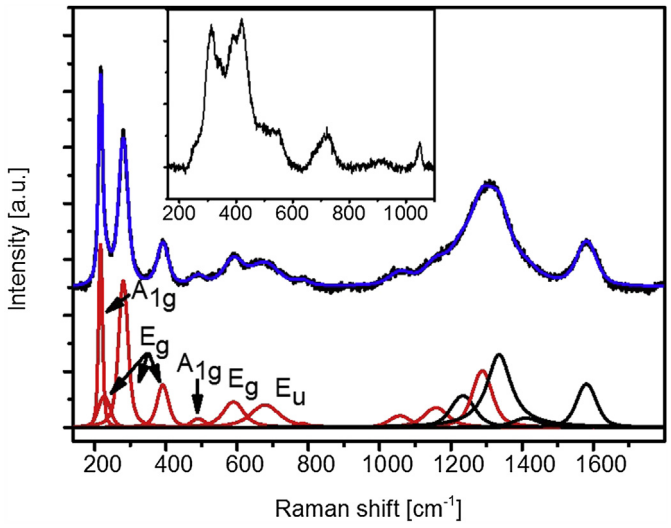

Fig. 2. Raman spectrum of HR/NCNTs/CP structure after heat treatment at 450 °C for 1 h. Note that the spectrum has been fitted (blue line) with two distinct components corresponding to the spectra of hematite (red line) and of carbon nanotubes (black line), respectively. The inset depicts the Raman spectrum of the as grown material before the heat treatment. (For interpretation of the references to color in this figure legend, the reader is referred to the web version of this article.)

and 289 cm^{-1}, demonstrate the successful transformation of iron hydroxide into hematite. A fitted spectrum (using Voigtian line shapes) is also shown in Fig. 2 with red (α-Fe_2O_3) and black (NCNTs) components in order to facilitate the assignment of the various peaks related to the different materials. The peaks are reported at the bottom of the same figure. A comprehensive table with all the details of the Raman spectra is reported separately (See Table S1 in supporting information).

The presence of single-phase hematite nanorods on the NCNTs is further supported by X-ray photoelectron spectroscopy (XPS). Fig. 3a displays a typical XPS spectrum of HR/NCNTs/CP. Strong Fe 2p and O 1s signals can be seen together with fairly weak peaks from carbon and nitrogen atoms in the NCNTs. The latter are explained by the rather thick and dense coating of the Fe_2O_3 'needles' on the surface of the NCNTs.

To better display the actual features originating from NCNTs, a typical XPS spectrum of NCNTs/CP is shown in Fig. 3b together with the high resolution XPS spectrum of N 1s shown as inset. Generally, the N 1s signal of the synthesized NCNTs/CP can be deconvoluted into four peaks at 398.4 eV, 399.5 eV, 400.8 eV, 401.9 eV representing different chemical bonding states and a tail at high binding energies due to $\pi-\pi$ interaction, which is typically observed in carbon systems. The two main N-peaks can be assigned to pyridinic and N-Q_{centre} functionalities [43], in line with earlier reports. From the XPS data a nitrogen atomic concentration of about 5.5% can be measured.

Mapping the HR/NCNTs/CP by energy dispersive X-ray spectroscopy (EDX) supports the XPS results and signals the presence of carbon, iron, oxygen and titanium. A more detailed analysis displays a strong signal of iron and oxygen which follows the NCNT structure confirming the attachment of hematite nanorods on the NCNTs (see Fig. S1 in supporting information).

An overview image of the surface of the hybrid material including iron oxide is presented in Fig. 1h. From the SEM images, the transition from iron hydroxide to hematite does not reveal any significant difference for the associated morphology; all the NCNTs are still completely covered by the nanorods grown vertically out from the surface of the NCNTs (see also Fig. S2 in supporting information).

Some HR/NCNTs were also scratched away from the surface of the CP to examine more in detail the structure of the nanorods by TEM. Fig. 4a and b show the TEM micrographs of HR/NCNTs before and after the heat treatment, respectively. Before the heat treatment it is clear that the iron hydroxide rods are formed as extremely thin needles, which align into bundles, making it difficult to precisely measure the diameter of each rod. A rough estimation indicates that the individual needles have diameters of few nanometers. After the heat treatment, the TEM image in Fig. 4b reveals the transformation of iron hydroxide into hematite as a loss of the sharp needle morphology which is instead replaced by a "finger-like" shape. The hematite nanorods also show some features of porosity after the heat treatment. Nevertheless, their morphology is relatively unchanged and all the nanorods are still well attached in a perpendicular-like orientation to the NCNTs.

The porosity of the nanorods after the heat treatment may result from the vaporization of some trapped water bubbles, which suggests that the phase transformation of iron hydroxide into hematite takes place by dehydration according to the following reaction [44]:

$$2FeOOH \rightarrow Fe_2O_3 + H_2O \quad (2)$$

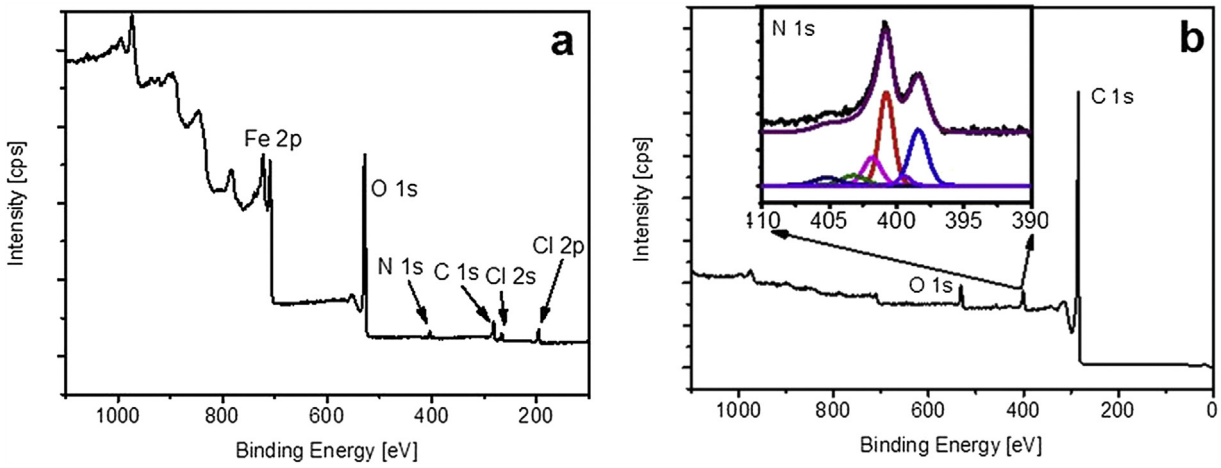

Fig. 3. XPS survey spectra of HR/NCNTs/CP with assigned peaks (a) and of NCNTs/CP (b). The inset presents a high resolution spectrum of the N 1s peak that has been deconvoluted into distinct peaks with different binding energies.

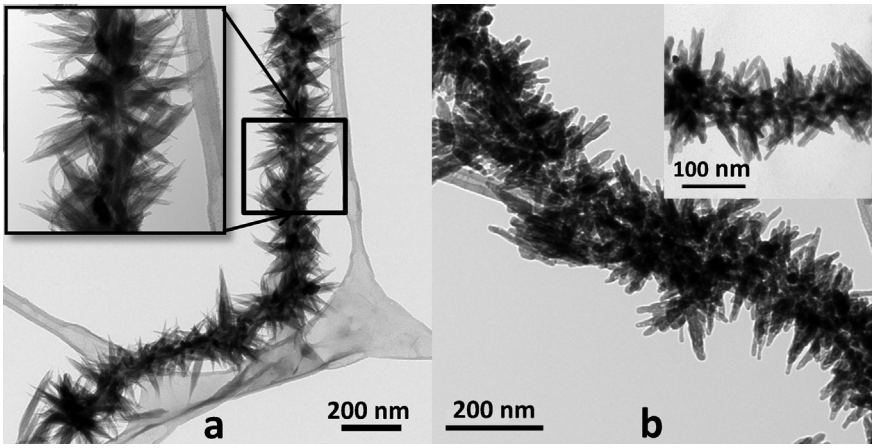

Fig. 4. TEM micrographs of the HR/NCNTs scraped from the CP substrate. Images of the materials obtained before the heat treatment (a) and after annealing at 450 °C for 1 h (b). Note the transformation from very sharp needles into more rounded 'finger-like' nanostructures.

A closer inspection of the porous nanorods shows that the water evaporation leads to pores with a maximum diameter of about 4.5 nm. One might speculate that this could further improve the Li storage capacity due to a larger reactive area, provided that the electrolyte can be infiltrated effectively into such small pores.

The crystallinity of the two HR/NCNTs/CP samples treated at 450 °C for different times (10 min and 1 h) was studied by means of Raman spectroscopy, since XRD (see Fig. S3) did not prove a suitable approach to identify and study the hematite nanostructures, due to their small crystal domain size and/or their low degree of crystallinity. The full width half maximum (FWHM) of all the hematite-related peaks in the Raman spectra decreases in correspondence of a longer duration of the heat treatment for the material (see Table S1). This is related to an increase in the crystalline domain size [45].

The loading of hematite on NCNTs/CP was determined by thermogravimetric analysis (TGA) on samples with and without hematite nanorods (Fig. S4). A typical loading of 0.2 mg/cm^2 of Fe_2O_3 was derived.

3.2. Electrochemical analysis of the hierarchical electrode materials

3.2.1. Cyclic voltammetry

Fig. 5 presents the results obtained for the cyclic voltammetry (CV) analysis conducted on the various electrodes at 0.05 mV s^{-1} between 0.05 and 3.0 V *vs.* Li^+/Li. Each graph in Fig. 5 refers to the first three cycles of a blank CP substrate (a); a NCNTs/CP electrode (b); a HR/NCNTs/CP hierarchical structure formed after 10 min at 450 °C (c); and an analogous HR/NCNTs/CP assembly obtained after 1 h at 450 °C (d), respectively.

From Fig. 5a it is clear that the blank CP substrate is *electroactive*, displaying typical red-ox signatures below 1.20 V *vs.* Li^+/Li. The peak marked as '0' around 0.75 V in all the different voltammograms can be related to the formation of a solid-electrolyte interphase (SEI) layer, due to the reduction of the electrolyte upon the first cathodic scan for the respective electrodes. This peak is distinctive for all the materials and its position and intensity are characteristic for the first half cycle of reduction, thus indicating that such irreversible process occurs in the initial phase of cycling. The blank CP shows a weak SEI-related feature, especially when compared to those of the HR/NCNTs/CP hierarchical structures, where the SEI layer is generated simultaneously with the conversion of Fe_2O_3 into Fe nanoparticles surrounded by a Li_2O matrix [22]. The coulombic efficiencies calculated from the areas subtended to the respective anodic/cathodic curves in the first cycle of the different electrodes yield 83% for the CP, 87% for the NCNTs/CP, and 80% and 74% for the HR/NCNTs/CP grown with different annealing times of 10 min and 1 h.

The presence of NCNTs has a very positive effect on charge recovery, especially considering that hematite suffers from scarce electrical conductivity and ultimately from poor reversibility. A couple of red-ox peaks can be noticed in all the voltammograms at low voltage, which are labeled as 'I' upon reduction (*i.e.* Li^+ uptake) and 'II' during oxidation (Li^+ release). These features are characteristic of graphitic materials and correspond to the insertion (or extraction) of Li^+ in such structures. Therefore, it is not possible here to distinguish clearly the features of the CP from those of the NCNTs/CP, since multi-walled NCNTs display very similar signatures [46]. Moreover, two other weak red-ox features (*i.e.* '0*' and 'III') are found for all the electrode materials around 1.0 V upon subsequent cycling in their cathodic and anodic parts of the curve, respectively. It can be seen that for both CP and NCNTs/CP the latter are distributed in a nearly symmetrical way, exhibiting a broad line shape. On the other hand, the peak '0*' is sharper for the HR/NCNTs/CP hierarchical structures due to the conversion reaction taking place in the hematite nanostructures.

The main differences that can be noticed comparing the CV cycles of the HR/NCNTs/CP structures with those of the carbonaceous electrodes (*i.e.* CP and NCNTs/CP) are the two extra oxidative features (*i.e.* 'IV' and 'IV_s') due to the sequential (*i.e.* two-stage) $Fe^0 \rightarrow Fe^{2+} \rightarrow Fe^{3+}$ oxidation [47,48], which extend approximately from 1.40 up to 2.20 V in the anodic part of their cycles. Furthermore, the weak bending of the cathodic part of the curves around 1.65 V (labeled by '#') corresponds to the initial stage of insertion of Li^+ into Fe_2O_3 forming $Li_xFe_2O_3$ (with $0 < x < 2$) [49,50].

It is clear that the main red-ox peaks at low voltage are enhanced by the presence of the NCNTs bound on the CP surface for the deposited electrodes. In particular, a satellite peak of reduction appears in the various voltammograms around 0.20 V (see colored arrows) after the first cycle. The shape and the intensity of the latter are particularly pronounced for the NCNTs/CP electrode and can be associated to the progressive Li storage in the inter-wall space of the NCNTs [10], which has been shown by HR-TEM to occur at low voltage *vs.* Li^+/Li [11]. The voltammograms in Fig. 5 clearly demonstrate that the overall charge stored upon Li^+ uptake/release increases upon progressive inclusion of the NCNTs and additional Fe_2O_3 nanorods with a consolidate structure.

The charge storage contribution associated to the conversion

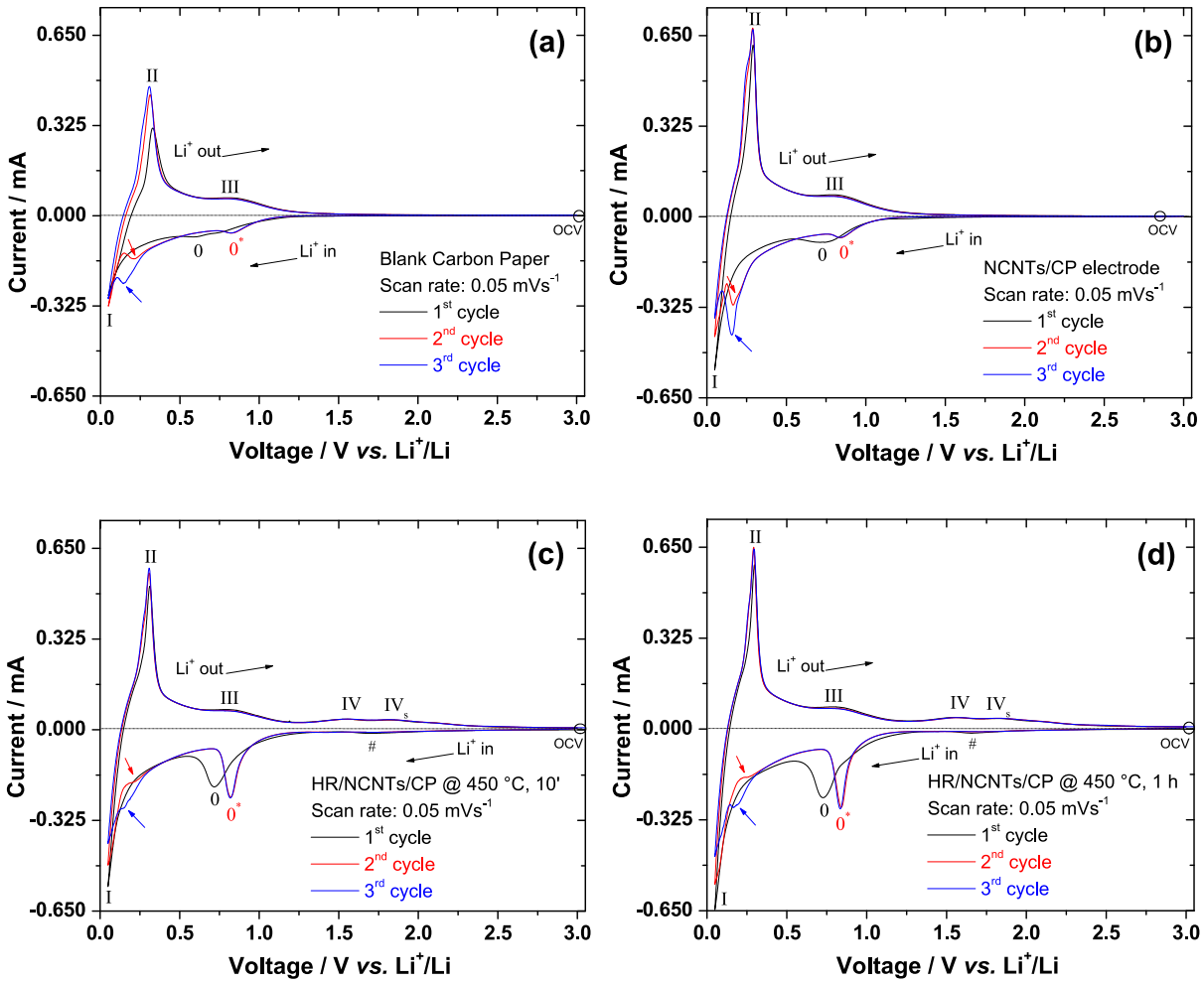

Fig. 5. Cyclic voltammograms of the different electrodes scanned between 0.05 and 3.0 V *vs.* Li^+/Li with a sweep rate of 0.05 mV s^{-1}. Initial CV cycles of a blank CP substrate (a); a NCNTs/CP electrode (b); a HR/NCNTs/CP hierarchical structure resulting from a thermal treatment of 10 min at 450 °C (c) and an analogous HR/NCNTs/CP electrode obtained after 1 h at 450 °C (d). The various peaks are labeled in the voltammograms. The asterisk refers to peaks obtained after the first cycle.

mechanism of Fe_2O_3 in the hierarchical structures can be appreciated more clearly in Fig. 6, when the same electrodes are subjected to subsequent CV cycles at increasing scan rates.

The oxidation band between 1.4 and 2.2 V in the anodic part of the cycle becomes progressively more prominent, as well as the extended contribution in the cathodic region below 1.0 V down to 0.05 *vs.* Li^+/Li, which overlaps the reductive processes associated to the NCNTs/CP. These wide red-ox bands, which extend well below and above the theoretical value of the standard potential associated to bulk Fe_2O_3 upon reaction with Li^+ ions (*i.e.* 1.62 V *vs.* Li^+/Li), are associated to a size distribution of the hematite nanostructures. The latter undergo electrochemical milling upon progressive conversion and de-conversion, thus generating a broad range of reaction potentials for the differently sized nanostructures [3]. The impact of these size effects on the electrochemical activity of the hierarchical HR/NCNTs/CP structures is evident in Fig. 6. In fact, the enhanced double layer charging in these cycles at increasing scan rates is clearly noticed, when compared to those analogously obtained for the NCNTs/CP and blank CP electrodes. The electrochemical response of the hematite nanostructures becomes more pronounced at higher scan rates, thus implying a more efficient charge storage combining both double layer charging and faradaic reactions over a broad range of potentials [3].

A careful analysis of the evolution of the peak potentials and the peak currents with the scan rates for the different electrodes was carried out as well. The results are reported separately in the Supporting Information (see Figs. S5, S6 and S7) and demonstrate that in all the cases both the oxidative and the reductive features in their associated half cycles shift towards more positive (*i.e.* for the anodic peaks) and more negative (*i.e.* for the cathodic peaks) potentials with increasing scan rates, respectively. Such behavior is normally related to processes limited by the rate of charge transfer and/or ohmic drop [51,52]. In particular, if a substantial *IR*-drop affects such electrochemical system, a linear relationship between the peak potential (E_p) and the scan rate can be expected on the basis of Ohm's law [52]. In this case, all the peak potentials referring to the different red-ox signatures in the various electrodes vary linearly with the square root of the applied scan rates (see Figs. S5, S6 and S7), possibly leaving charge transfer as the main limiting step and supporting the idea that the reactions are kinetically controlled.

Interestingly, the behavior of the peak current (I_p) related to reduction and oxidation displays different trends, depending on the type of electrode and its particular electrochemical process. For example, the peak current due to the cathodic peak '0*' in the various voltammograms for the four electrodes exhibits different evolutions with the scan rate, as its absolute value is proportional to the scan rate for both CP and NCNTs/CP, whereas it shows a linear

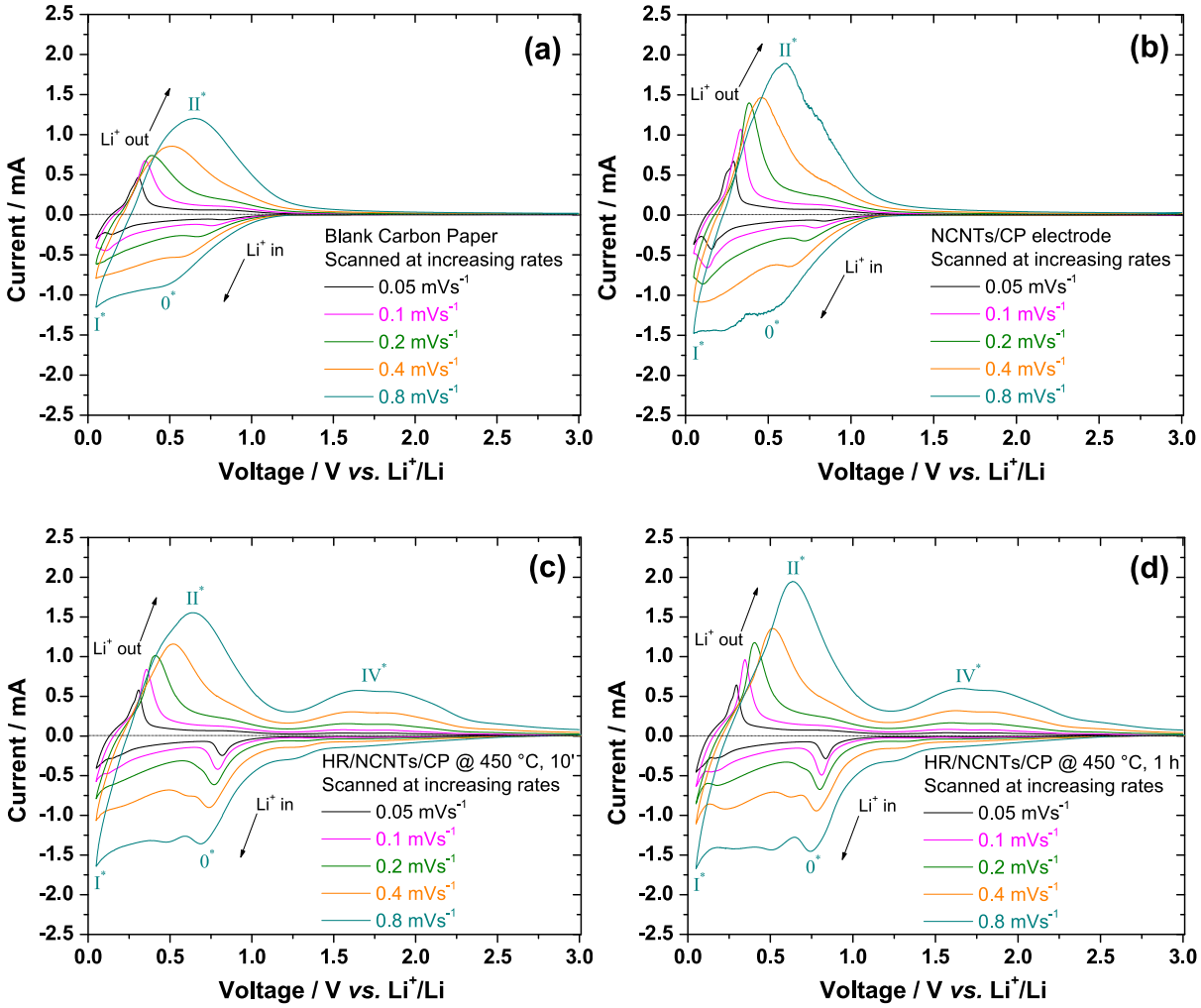

Fig. 6. Cyclic voltammograms of the various electrode structures scanned between 0.05 and 3.0 V *vs.* Li^+/Li at increasing sweep rates. Note that the cycles in all the graphs are subsequent to those shown in the previous figure and the peaks are marked with an asterisk for this reason.

relationship with the square root of the sweep rate for both the hierarchical HR/NCNTs/CP structures. This fact suggests that the reduction reactions in both CP and NCNTs (*i.e.* both involving only Li^+ insertion) occur under thin film electrochemical conditions [51,52] and thus these processes are surface-controlled. Vice versa, the reduction mechanism for both the hierarchical HR/NCNTs/CP structures appears to be limited by diffusion, as indicated by the characteristic dependence of the current from the reciprocal of the square root of time (*i.e.* $\sqrt{mVs^{-1}}$). This could be rationalized on the fact that major structural changes are involved in the conversion reaction through the Fe_2O_3 'needles' densely grown on the NCNTs 'branches', which then affect the transport of the charge carriers. Concurrently, the oxidation feature 'II*' at low voltage *vs.* Li^+/Li shows a clear non-linear behavior for the current peaks in all the different plots in Fig. S6 extracted from the voltammograms in Fig. 6. This unusual characteristic is not fully understood and it could be due to the particular properties of the CP substrate, as this trait is noticed for all the different electrodes.

Finally, the oxidation feature 'VI*' associated to the de-conversion process and the first stage of Fe_2O_3 regeneration shows a surface-controlled behavior, manifested by I_p being proportional to the scan rate. This is quite surprising, since this de-conversion step involves structural changes as well. The close contact of the reacting nanostructures with the NCNTs and the electrochemical milling process of Fe_2O_3 could contribute in minimizing the diffusion distance for the charge carriers. Nonetheless, the electrochemical grinding mechanism could also cause progressive interface degradation, which could become a limiting factor in this way. In any case, this behavior further confirms the asymmetries existing for hematite during its reduction and oxidation reactions.

3.2.2. Galvanostatic tests

The hierarchical structures containing NCNTs/CP and HR/NCNTs/CP grown at 450 °C with different times of 10 min and 1 h were also subjected to galvanostatic cycling using a constant current density of 0.3 mA cm^{-2}, which here corresponded approximately to an initial C-rate of C/5 for all the three electrodes. The voltage profiles of discharge and charge for these electrodes are shown in Fig. 7.

From the various profiles in Fig. 7 it is easily noticed that the characteristic red-ox features discussed earlier in Fig. 5 are matched by the plateaus and the inflections found in the respective discharge/charge curves. In particular, the NCNTs/CP displays only a weak bump around 0.7 V due to SEI layer formation, whereas pronounced plateaus are observed for the HR/NCNTs/CP, especially for the structure grown at 450 °C for 1 h. The coulombic efficiencies for the first discharge/charge cycle are 82.0% for the NCNTs/CP, whereas 82.3% and 74.0% for the HR/NCNTs/CP grown for 10 min

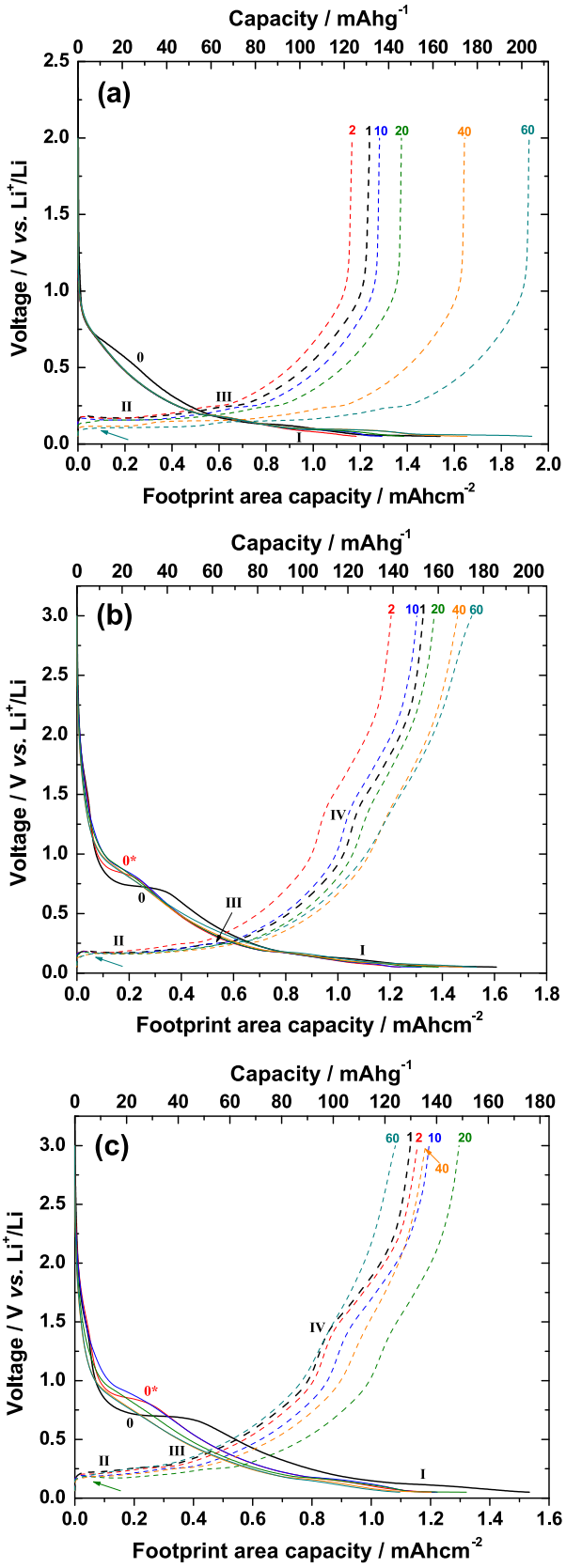

Fig. 7. Galvanostatic discharge (solid lines) and charge (dotted lines) profiles obtained for the hierarchical structures containing respectively NCNTs/CP (a); HR/NCNTs/CP grown at 450 °C for 10 min (b); and HR/NCNTs/CP formed after 1 h at 450 °C (c). Note that all the electrodes have been tested applying a constant current density of 0.3 mA cm^{-2}. The NCNTs/CP electrode has been cycled between 0.05 and 2.0 V *vs.* Li^+/Li, whereas both HR/NCNTs/CP structures have been discharged and charged between 0.05 and 3.0 V to allow full regeneration of the iron oxide nanostructures. The asterisk refers to red-ox features obtained after the first cycle. Note that the capacities are reported per footprint area for convenience, since it is not possible to clearly separate the various contributions from the different active materials. The values of the gravimetric capacities are referred in each case to the *total mass* of the entire electrode.

and 1 h, respectively. In the NCNTs/CP voltage profiles of Fig. 7a, a typical 'staging' with plateaus and steps in both the discharge and charge curves can be noticed at low voltage. The latter is characteristic for intercalation in graphitic hosts (see also Supporting information, Fig. S9). The energy efficiencies of the first charge/discharge cycle have been calculated from the associated curves. Their values are 81.2% for NCNTs/CP, whereas 64.3% and 64.4% for HR/NCNTs/CP grown for 10 min and 1 h, respectively.

Comparing the three voltage profiles in Fig. 7 it is clear that the NCNTs/CP electrode offers the best combination in terms of average reaction potential, coulombic and energy efficiencies. As a matter of fact, the conversion/de-conversion process requires additional energy for the continuous formation and rearrangement of the interfaces in the Fe/Li_2O nanocomposite and the regenerated Fe_2O_3 nanostructures. Moreover, the necessity of utilizing a higher upper cut-off voltage of 3.0 V *vs.* Li^+/Li to recover most of the capacity deriving from the de-conversion mechanism has also some detrimental effects. The latter not only affects the average operational voltage, but it could also trigger some parasitic processes in these electrodes, since the exposed surface area of the Fe_2O_3 'needles' in direct contact with the electrolyte is relevant in this type of 3D architecture.

The NCNTs/CP electrode provides the best electrochemical performance and its footprint area capacities increase upon progressive cycling up to about 1.95 mAh cm^{-2} (*i.e.* ≈204 mAh g^{-1} referring to the mass of the *entire electrode*) after 60 cycles with an excellent coulombic efficiency. Most of the discharge/charge capacities are delivered below 1.20 V, in agreement with the previous measurements. The discharge and charge capacities rise well beyond their initial values (e.g. 1.55 mAh cm^{-2}), as a result of the defects induced by the N-doping, which progressively open the way to the additional Li storage in the inter-wall regions of the NCNTs. The discharge curves retain their typical shape upon subsequent cycling and it is the length of their last two 'steps' at low voltage that are extended. Vice versa, the corresponding charge curves display profiles that do not overlap and that widen with increasing cycle number. The initial voltage step around 0.20 V upon charge becomes shallower as a function of higher cycle numbers (see colored arrow), while the extension of the plateaus grows, thus conferring a flatter profile to the curves in this potential region. These performances are remarkable, especially considering that the cycling is carried out at a current density of 0.3 mAcm^{-2} on rather thin electrode structures. Indeed, the values of the footprint area capacity are comparable with those of 3D carbon-network electrodes based on significantly thicker porous carbonaceous materials tested under similar cycling conditions [53].

The discharge and charge curves for the HR/NCNTs/CP in Fig. 7b and c exhibit similar profiles, where the distinctive signature of the NCNTs/CP structure is superimposed to that of the conversion ('0*') and de-conversion ('IV') occurring in the hematite needles. Also in these cases the capacity increases, although the trend is slightly different for the two hierarchical structures. The HR/NCNTs/CP electrode grown at 450 °C for 10 min displays a rise of the capacity as a function of cycling, where the shape of the discharge/charge curves becomes more sloping in the potential regions associated to the conversion/de-conversion reactions. The characteristic red-ox features '0*' and 'IV' become less pronounced and stretched over

a large voltage window, in correspondence of the electrochemical milling process occurring in the Fe_2O_3 nanostructures. The charge curves in Fig. 7b become straighter in the high voltage region after 40 cycles and the associated discharge/charge capacities rise up to about 1.54 mAh cm^{-2} (e.g. ≈175 mAh g^{-1} referred to the mass of the *entire electrode*) after 60 cycles. Also in this case, the capacity per footprint area has been utilized to assess the performance of the electrode, since it is difficult to determine accurately the individual weight percentages of the active materials, considering also that each component of these hierarchical structures participates in the reactions. Therefore, the differences observed for the capacities of the three electrodes in Fig. 7 can be likely due to the discrepancies in the various masses of the HR/NCNTs coatings, as well as to some slight deviations in the mass of the pristine CP substrates. Nevertheless, the electrochemical behavior of each electrode is distinctive and it can be seen also that in Fig. 7c the initial reversibility of the HR/NCNTs/CP electrode treated for 1 h at 450 °C is higher than that shown in Fig. 7b by the analogous structure formed with a 10 min treatment. However, after a preliminary capacity enhancement during the first 20 cycles, an onset of charge loss is observed. This is particularly visible in the charge profiles. The latter become steeper and yield limited capacity values.

The evolution of the discharge/charge capacities of the various electrodes upon cycling at 0.3 mA cm^{-2} is presented in Fig. 8, where the cycle performance of a blank CP substrate, tested with the same current density, has been included as reference.

It is clear from Fig. 8 that coating the CP has a positive impact on raising the capacities for the resulting hierarchical structures. A large capacity retention improvement is achieved only when the NCNTs are deposited on the CP support. The dense coverage of hematite nanorods could also constitute a limiting factor for the performance of the overall electrodes, for the reasons mentioned earlier and also considering the moderate conductivity of the CP. It should be noted also that the dense attachment of the hematite nanostructures onto the defects induced by the N-doping could hinder the accessibility of the latter, which are crucial for achieving Li storage into the inter-wall regions of the NCNTs [11]. The initial good performance of the blank CP starts fading after 35 cycles and

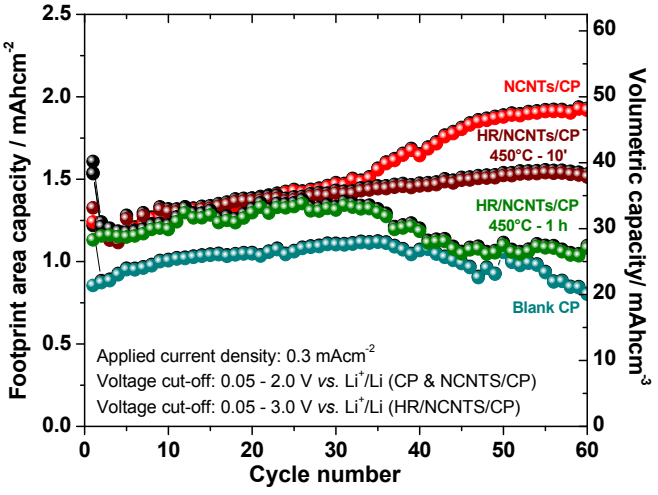

Fig. 8. Cycle performance of the various electrode structures upon galvanostatic cycling at 0.3 mA cm^{-2}. The evolution of the discharge (black circles) and charge (colored circles) footprint area capacities for the hierarchical structures are compared with those of a blank CP substrate cycled under analogous conditions. Note that the HR/NCNTs/CP electrodes have been charged to a higher potential (*i.e.* 3.0 V *vs.* Li^+/Li) than that applied to CP and NCNTs/CP. (For interpretation of the references to color in this figure legend, the reader is referred to the web version of this article.)

the trends of the capacities associated to the NCNTs/CP and the HR/NCNTs/CP structure grown with the shorter thermal treatment are clearly deviating from the charge losses experienced by the carbonaceous support. This is a further proof of the positive effect of the N-doping of the nanotubes and their role in promoting the electrical conductivity of the hierarchical electrodes and their overall electrochemical response.

As far as the differences between the two HR/NCNTs/CP electrodes are concerned, this could be due to a different degree of crystallinity or consolidation of the hematite nanostructures formed at 450 °C, as a consequence of the diverse duration of their thermal treatments, as deduced from Raman spectroscopy. Since the conversion mechanism implies a radical change of the structure and the size of the hematite, as well as its amorphization in the early formation of the Fe/Li_2O nanocomposite, it is reasonable that hematite needles with a reduced crystal domain size, a higher defect concentration and a smaller particle size could undergo these reactions in a more favorable way. In fact, the continuous electrochemical milling process can start from a point where the reacting material can be sub-divided further without an excessive energy expense to promote the formation of new phase boundaries.

Additional galvanostatic tests were also performed on the NCNTs/CP and the HR/NCNTs/CP structures after the CV analyses shown in Figs. 5 and 6, in order to further clarify the discrepancies observed for these electrodes. The results are separately presented in Figs. S9, S10 and S11 in the supporting information. The various graphs in the supplementary figures present the electrochemical behaviors exhibited by these electrodes when they are cycled with the same current density of 0.1 mA cm^{-2}. This corresponded to an initial C-rate of about C/20.5 for NCNTs/CP, C/22.3 for HR/NCNTs/CP treated for 10 min at 450 °C and C/23.6 for the analogous hierarchical structure obtained at 450 °C after 1 h, respectively. Also in this case, the data refer to the specific footprint area capacity and to the overall volumetric capacity of the electrodes, which are the figures of major importance for miniaturized Li-ion microbattery systems.

The main results for the data presented in the Supporting Information are briefly mentioned here. The NCNTs/CP electrode yields characteristic 'graphitic' plateaus associated to the Li staging in these carbonaceous structures, which are preserved upon progressive cycling (Fig. S9a). The footprint area capacities after 20 cycles are about 2.1 mAh cm^{-2}, which roughly corresponds to 51 mAh cm^{-3} (see Fig. S9b). Both coulombic and energy efficiencies display excellent values of 100.0% and 85.0% after 20 cycles, as well as very limited shifts in the incremental capacity at the cut-off voltage points (*i.e.* 0.05 and 2.0 V) in Fig. S9a. Vice versa, the discharge/charge profiles for both the HR/NCNTs/CP structures (Figs. S10a and S11a) show a larger hysteresis, as well as a continuous shift of the incremental capacities at 0.05 V and 3.0 V, respectively. These phenomena are due to the conversion reaction and the electrochemical milling, which further enhances the red-ox activities of the nanoparticles. The shift in the incremental capacities could be connected also to some parasitic mechanism triggered by the increasing interfacial area (see also Fig. S8), ultimately limiting the coulombic efficiency for these systems. In this respect, some previous studies [54–56] have pointed out that the uncoated surface of compounds undergoing conversion reactions is likely the cause behind their limited coulombic efficiencies. Therefore, the overall capacity increases upon electrochemical milling, however, the coulombic efficiency is lower than that obtained by the NCNTs/CP alone. The discharge/charge capacities per footprint area are rather stable for both electrodes (see Figs. S10b and S11b) with values of about 2.25 mAh cm^{-2} and volumetric capacities around 60 mAh cm^{-3}. The final values for the respective coulombic and

energy efficiencies after 20 cycles are 98.3% and 60.9% for the sample treated at 450 °C for 10 min, whereas 97.9% and 61.1% for that annealed for 1 h. In any case, such figures are not comparable with those obtained by the NCNTs/CP, which should be preferred for use in an advanced 3D negative electrode with improved performances.

4. Conclusions

As a means of producing a versatile negative electrode on a metal-free current collector for Li-ion batteries and 3D microbatteries, hierarchical self-assembled structures relying on carbon paper (CP) and multi-walled (MW) nitrogen-doped carbon nanotubes (NCNTs) have been formed and further functionalized with hematite nanostructures attached on their outer walls producing a "tree-like" electrode morphology. The electrochemical behavior and the footprint area capacities of these 3D architectures were investigated to probe their applicability as negative electrodes for Li-ion microbatteries. Nevertheless, this type of electrodes could be up-scaled also for conventional Li-ion batteries, due to the promising electrochemical characteristics of the NCNTs, which intrinsically combine high specific energy and power densities, as well as the possibility of further increasing the footprint area capacities by a double-side coating of the carbon paper support.

N-doped carbon nanotubes on carbon paper (NCTNs/CP) displayed footprint area capacities as high as 2.1 mAh cm^{-2} at 0.1 mA cm^{-2} after 20 cycles and up to 1.95 mAh cm^{-2} after 60 cycles at 0.3 mA cm^{-2} showing in both cases excellent coulombic and energy efficiencies. Vice versa, the cycle performances of the HR/NCNTs/CP structures incorporating the hematite nanorods increased the footprint area capacity roughly up to 2.25 mAh cm^{-2} at 0.1 mA cm^{-2}, however, their coulombic and energy efficiencies were not as good as those provided by the NCNTs/CP alone. This is due to the nature of the conversion reaction occurring in the Fe_2O_3 nanostructures, which causes a continuous rearrangement of the phase boundaries, as well as a progressive electrochemical milling. A similar initial rise in capacity was observed for the HR/NCNTs/CP and the NCNTs/CP structures upon cycling. This was also confirmed by cycling at a higher current density of 0.3 mA cm^{-2}, where the differences with the NCNTs/CP electrode became more evident after the first 40 cycles, likely due to surface deterioration in the HR/NCNTs/CP structures. In general, the values of the footprint area capacity are comparable with those of other 3D carbon-network electrodes based on significantly thicker porous carbonaceous materials tested under similar cycling conditions.

The N-doping of the CNTs proved here to be the key for high energy density and power performances by the generation of defects on the CNT walls, which act as preferential adsorption sites for the Li^+ ions. The N-doping causes also a progressive capacity increase, because the defects in the MW-NCNTs open the way for Li storage into the innermost inter-wall regions, which are not immediately accessible in analogous undoped CNTs. These defects provide also favorable nucleation centers to initiate the growth of the iron oxide nanostructures to obtain a complete hierarchical assembly.

Furthermore, the entire electrode structure has been designed to be active with the carbon paper support participating in the electrochemical reactions. The NCNTs represent in fact an extension of the carbon fibers in the underlying substrate providing a larger surface area available for the electrochemical reactions, especially when the hematite nanorods are attached to their defective walls.

This study clearly demonstrates that the Li storage in the NCNTs occurs *via* a highly reversible insertion mechanism, which generates characteristic 'graphitic staging' at low voltage *vs.* Li^+/Li. The staging plateaus become more defined and extended with increasing cycle number causing a rise of the discharge/charge capacities, as well as smoother transitions with the adjacent steps. For these reasons the NCNTs/CP electrodes should be preferred over the HR/NCNTs/CP structures as efficient negative electrodes for both Li-ion batteries and 3D microbatteries. Finally, the design of the HR/NCNTs/CP structures could be suitable for boosting the surface reactivity of the resulting materials, which, for example, could be applied to supercapacitors, thus avoiding the limitations imposed by the conversion reactions and exploiting the larger surface areas provided by their hierarchical architecture. The latter could also find application in other technological fields such as advanced sensors or for catalysis.

Acknowledgments

This work was supported by the Artificial Leaf Project Umeå (K&A Wallenberg foundation) and by the Swedish Research Council (Grant dnr 2013-5252). T. W. thanks Ångpanneföreningen for support. T. S. thanks Kempe foundation for support. We acknowledge Umeå Core facility for Electron Microscopy (UCEM). The electron microscopy H. Eriksson is gratefully acknowledged for his technical support.

Appendix A. Supplementary data

Supplementary data related to this article can be found at http://dx.doi.org/10.1016/j.jpowsour.2015.01.036.

References

[1] K. Edström, D. Brandell, T. Gustafsson, L. Nyholm, Electrochem. Soc. Interface 20 (2011) 41–46.
[2] M. Roberts, P. Johns, J. Owen, D. Brandell, K. Edstrom, G. El Enany, C. Guery, D. Golodnitsky, M. Lacey, C. Lecoeur, H. Mazor, E. Peled, E. Perre, M.M. Shaijumon, P. Simon, P.L. Taberna, J. Mater. Chem. 21 (2011) 9876–9890.
[3] M. Valvo, D. Rehnlund, U. Lafont, M. Hahlin, K. Edström, L. Nyholm, J. Mater. Chem. A 2 (2014) 9574–9586.
[4] D. Golodnitsky, M. Nathan, V. Yufit, E. Strauss, K. Freedman, L. Burstein, A. Gladkich, E. Peled, Solid State Ion. 177 (2006) 2811–2819.
[5] A.S. Arico', P. Bruce, B. Scrosati, J.M. Tarascon, W. Van Schalkwijk, Nat. Mater. 4 (2005) 366–377.
[6] P.G. Bruce, B. Scrosati, J.M. Tarascon, Angew. Chem. Int. Ed. 47 (2008) 2930–2946.
[7] M. Valvo, E. García-Tamayo, U. Lafont, E.M. Kelder, J. Power Sources 196 (2011) 10191–10200.
[8] P.L. Taberna, S. Mitra, P. Poizot, P. Simon, J.M. Tarascon, Nat. Mater. 5 (2006) 567–573.
[9] M. Valvo, M. Roberts, G. Oltean, B. Sun, D. Rehnlund, D. Brandell, L. Nyholm, T. Gustafsson, K. Edström, J. Mater. Chem. A 1 (2013) 9281–9293.
[10] X. Li, J. Liu, Y. Zhang, Y. Li, H. Liu, X. Meng, J. Yang, D. Geng, D. Wang, R. Li, X. Sun, J. Power Sources 197 (2012) 238–245.
[11] W.H. Shin, H.M. Jeong, B.G. Kim, J.K. Kang, J.W. Choi, Nano Lett. 12 (2012) 2283–2288.
[12] L.G. Bulusheva, A.V. Okotrub, A.G. Kurenya, H. Zhang, X. Chen, H. Song, Carbon 49 (2011) 4013–4023.
[13] C.C. Kaun, B. Larade, H. Mehrez, J. Taylor, H. Guo, Phys. Rev. B Condens. Matter Mater. Phys. 65 (2002) 2054161–2054165.
[14] S. Latil, S. Roche, D. Mayou, J.C. Charlier, Phys. Rev. Lett. 92 (2004) 256801–256805.
[15] S.H. Lim, R. Li, W. Ji, J. Lin, Phys. Rev. B Condens. Matter Mater. Phys. 76 (2007).
[16] H.R. Barzegar, E. Gracia-Espino, T. Sharifi, F. Nitze, T. Wågberg, J. Phys. Chem. C 117 (2013) 25805–25816.
[17] F. Villalpando-Paez, A. Zamudio, A.L. Elias, H. Son, E.B. Barros, S.G. Chou, Y.A. Kim, H. Muramatsu, T. Hayashi, J. Kong, H. Terrones, G. Dresselhaus, M. Endo, M. Terrones, M.S. Dresselhaus, Chem. Phys. Lett. 424 (2006) 345–352.
[18] Z.R. Ismagilov, A.E. Shalagina, O.Y. Podyacheva, A.V. Ischenko, L.S. Kibis, A.I. Boronin, Y.A. Chesalov, D.I. Kochubey, A.I. Romanenko, O.B. Anikeeva, T.I. Buryakov, E.N. Tkachev, Carbon 47 (2009) 1922–1929.
[19] D. Quiñonero, A. Frontera, C. Garau, A. Costa, P. Ballester, P.M. Deyà, Chem. Phys. Lett. 411 (2005) 256–261.
[20] B. Yue, Y. Ma, H. Tao, L. Yu, G. Jian, X. Wang, Y. Lu, Z. Hu, J. Mater. Chem. 18 (2008) 1747–1750.
[21] E. Gracia-Espino, X. Jia, T. Wågberg, J. Phys. Chem. C 118 (2014) 2804–2811.
[22] P. Poizot, S. Laruelle, S. Grugeon, L. Dupont, J.M. Tarascon, Nature 407 (2000)

496–499.
[23] J. Cabana, L. Monconduit, D. Larcher, M.R. Palacín, Adv. Mater. 22 (2010) E170–E192.
[24] M. Armand, J.M. Tarascon, Nature 451 (2008) 652–657.
[25] W. Shi, X. Rui, J. Zhu, Q. Yan, J. Phys. Chem. C 116 (2012) 26685–26693.
[26] D. Li, D. Shi, Z. Chen, H. Liu, D. Jia, Z. Guo, RSC Adv. 3 (2013) 5003–5008.
[27] N. Du, H. Zhang, B. Chen, J. Wu, X. Ma, Z. Liu, Y. Zhang, D. Yang, X. Huang, J. Tu, Adv. Mater. 19 (2007) 4505–4509.
[28] Y. Wang, J. Xu, H. Wu, M. Xu, Z. Peng, G. Zheng, J. Mater. Chem. 22 (2012) 21923–21927.
[29] P. Balaya, Energy Environ. Sci. 1 (2008) 645–654.
[30] B. Ellis, P. Subramanya Herle, Y.H. Rho, L.F. Nazar, R. Dunlap, L.K. Perry, D.H. Ryan, Faraday Discuss. 134 (2007) 119–141.
[31] J. Jiang, Y. Li, J. Liu, X. Huang, C. Yuan, X.W. Lou, Adv. Mater. 24 (2012) 5166–5180.
[32] V.A.N. De Carvalho, R.A.D.S. Luz, B.H. Lima, F.N. Crespilho, E.R. Leite, F.L. Souza, J. Power Sources 205 (2012) 525–529.
[33] L. Vayssieres, N. Beermann, S.E. Lindquist, A. Hagfeldt, Chem. Mater. 13 (2001) 233–235.
[34] T. Sharifi, E. Gracia-Espino, H. Reza Barzegar, X. Jia, F. Nitze, G. Hu, P. Nordblad, C.W. Tai, T. Wågberg, Nat. Commun. 4 (2013).
[35] Y. Zhang, R. Zhu, Y. Cui, J. Zhong, X. Zhang, J. Chen, Nanotechnology 25 (2014) 135607.
[36] P. Kichambare, J. Kumar, S. Rodrigues, B. Kumar, J. Power Sources 196 (2011) 3310–3316.
[37] C.-L. Sun, C.-W. Pao, H.-M. Tsai, J.-W. Chiou, S.C. Ray, H.-W. Wang, M. Hayashi, L.-C. Chen, H.-J. Lin, J.-F. Lee, L. Chang, M.-H. Tsai, K.-H. Chen, W.-F. Pong, Nanoscale 5 (2013) 6812–6818.
[38] S.J. Oh, D.C. Cook, H.E. Townsend, Hyperfine Interact. 112 (1998) 59–65.
[39] H. Sjöström, S. Stafström, M. Boman, J.E. Sundgren, Phys. Rev. Lett. 75 (1995) 1336–1339.
[40] T. Sharifi, F. Nitze, H.R. Barzegar, C.W. Tai, M. Mazurkiewicz, A. Malolepszy, L. Stobinski, T. Wågberg, Carbon 50 (2012) 3535–3541.
[41] D.L.A. De Faria, S. Venâncio Silva, M.T. De Oliveira, J. Raman Spectrosc. 28 (1997) 873–878.
[42] A.M. Jubb, H.C. Allen, ACS Appl. Mater. Interfaces 2 (2010) 2804–2812.
[43] T. Sharifi, G. Hu, X. Jia, T. Wågberg, ACS Nano 6 (2012) 8904–8912.
[44] M.A. Chan, J. Ormö, A.J. Park, M. Stich, V. Souza-Egipsy, G. Komatsu, Geofluids 7 (2007) 356–368.
[45] V. Swamy, A. Kuznetsov, L.S. Dubrovinsky, R.A. Caruso, D.G. Shchukin, B.C. Muddle, Phys. Rev. B Condens. Matter Mater. Phys. 71 (2005).
[46] W. Ren, D. Li, H. Liu, R. Mi, Y. Zhang, L. Dong, Electrochim. Acta 105 (2013) 75–82.
[47] J. Morales, L. Sánchez, F. Martín, F. Berry, X. Ren, J. Electrochem. Soc. 152 (2005) A1748–A1754.
[48] M. Valvo, F. Lindgren, U. Lafont, F. Björefors, K. Edström, J. Power Sources 245 (2014) 967–978.
[49] M.M. Thackeray, W.I.F. David, J.B. Goodenough, Mater. Res. Bull. 17 (1982) 785–793.
[50] D. Larcher, C. Masquelier, D. Bonnin, Y. Chabre, V. Masson, J.B. Leriche, J.M. Tarascon, J. Electrochem. Soc. 150 (2003) A133–A139.
[51] A.K. Hjelm, G. Lindbergh, A. Lundqvist, J. Electroanal. Chem. 506 (2001) 82–91.
[52] S. Nordlinder, L. Nyholm, T. Gustafsson, K. Edström, Chem. Mater. 18 (2006) 495–503.
[53] H.D. Asfaw, M. Roberts, R. Younesi, K. Edström, J. Mater. Chem. A 1 (2013) 13750–13758.
[54] D. Bresser, E. Paillard, R. Kloepsch, S. Krueger, M. Fiedler, R. Schmitz, D. Baither, M. Winter, S. Passerini, Adv. Energy Mater. 3 (2013) 513–523.
[55] Z.S. Wu, W. Ren, L. Wen, L. Gao, J. Zhao, Z. Chen, G. Zhou, F. Li, H.M. Cheng, ACS Nano 4 (2010) 3187–3194.
[56] S. Grugeon, S. Laruelle, R. Herrera-Urbina, L. Dupont, P. Poizot, J.M. Tarascon, J. Electrochem. Soc. 148 (2001) A285–A292.